

**Constructing the Square-Like Copper Cluster to Boost C-C Coupling for CO₂
Electroreduction to Ethylene**

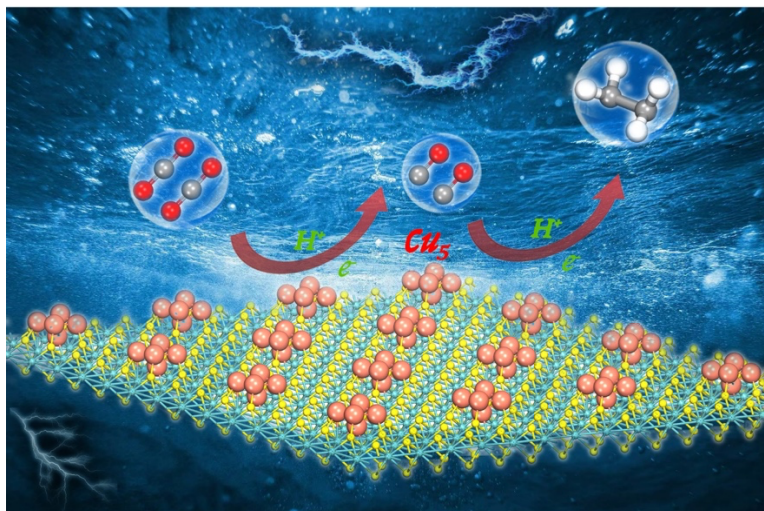
Tiantian Zhao,¹ Tingyu Yan,¹ Yuting Sun,¹ Zhongxu Wang,¹ Qinghai Cai,¹ Jingxiang
Zhao^{1,*} Zhongfang Chen^{2,*}

¹ *College of Chemistry and Chemical Engineering, and Key Laboratory of Photonic
and Electronic Bandgap Materials, Ministry of Education, Harbin Normal University,
Harbin 150025, China*

² *Department of Chemistry, University of Puerto Rico, Rio Piedras Campus, San Juan,
Puerto Rico 00931, USA*

* To whom correspondence should be addressed. Email: zhaojingxiang@hrbnu.edu.cn
(J. Z.); zhongfang.chen1@upr.edu (Z.C.)

TOC



Abstract: The CO₂ electroreduction reaction (CO₂ER) to ethylene (C₂H₄) offers the dual promise of lowering CO₂ emission while storing energy from renewable electricity, in which the development of highly efficient electrocatalysts is of great significance. Herein, by means of density functional theory (DFT) computations, we designed an electrocatalyst for CO₂-to-C₂H₄ conversion by anchoring the Cu₅ cluster supported on the MoS₂ monolayer with the S monovacancy (Cu₅@MoS₂). Our results revealed that one Cu atom of the Cu₅ cluster was embedded into the framework of the defective MoS₂ monolayer, while the other four Cu atoms form a square-like island over the substrate surface. Interestingly, the C–C coupling between two *CO species can easily occur on the unique square-like active site with a low kinetic barrier of 0.56 eV to form the key *C₂O₂ intermediate, which can then be hydrogenated to the C₂H₄ product with a very low limiting potential (–0.32 eV). Significantly, the alkaline condition (pH = 13) is beneficial to further promote C₂H₄ synthesis. Our work may offer a new avenue to precisely modulate the structures of the Cu clusters for converting CO₂ into high-value target products.

1. Introduction

Electrochemical reduction of carbon dioxide (CO₂ER) into value-added fuels and chemicals using excess renewable electricity has emerged as a promising strategy to address energy and environmental challenges.¹⁻³ Various hydrocarbons can be produced through CO₂ER, including methane (CH₄), formic acid (HCOOH), ethylene (C₂H₄), and ethanol (C₂H₅OH).⁴ Among these hydrocarbons, C₂H₄ holds particular significance in industrial applications due to its high value, transportability, and wide range of use in the production of plastics, solvents, and cosmetics.⁵⁻⁷ However, the CO₂-to-C₂H₄ conversion suffers from extremely low selectivity and catalytic activity due to the following substantial challenges:⁸⁻¹¹ 1) the competition with the inevitable hydrogen evolution reaction (HER); 2) the higher thermodynamic potential required for the formation of C₂H₄ compared to monocarbon (C₁) compounds, since the C₂H₄ formation involves a complex 12e⁻ pathway ($2\text{CO}_2 + 12\text{H}^+ + 12\text{e}^- \rightarrow \text{C}_2\text{H}_4 + 4\text{H}_2\text{O}$) and a multifaceted reaction network; 3) the difficult C-C coupling reaction between adjacent *CO(H) adsorbates, characterized by slow kinetics. To overcome these challenges, it is crucial to develop high performance electrocatalysts capable of achieving high selectivity at low potentials for the efficient production of C₂H₄ through CO₂ER.

To date, copper (Cu) has been widely recognized as a promising catalyst for the production of multicarbon (C₂₊) compounds, primarily due to its moderate adsorption strength with *CO intermediate.¹²⁻¹⁵ For example, Liu's group reported that Cu-based nanoneedles and grain boundary can promote the C-C coupling and enhance the catalytic activity of CO₂ER to C₂ products.¹⁶⁻¹⁹ However, the efficiency and selectivity

of Cu-based catalysts for C₂₊ products are far from satisfactory due to their high overpotentials, multiple products, inadequate selectivity, and poor stability under reaction conditions.²⁰⁻²² Especially, the surface structure of Cu crystals significantly influences C-C coupling reactions.²³⁻²⁵ For example, Cu(100) has been found to favor C₂H₄ formation, while CH₄ is preferentially generated from CO₂ER on Cu(111) surface.²⁶⁻²⁹ Consequently, developing novel Cu-based catalysts with high selectivity, activity, stability, and cost-effectiveness for the electrocatalytic conversion of CO₂ to C₂H₄ remains an appealing yet formidable challenge.

Note that the supported metal clusters (SMCs) have recently emerged as a special type of heterogeneous catalysts, comprising metal clusters stabilized on solid supports to serve as effective catalytic sites.^{30, 31} In particular, these SMCs catalysts possess adjacent metal sites, which exhibit an excellent synergistic effect in catalysis, crucial for achieving superior electrocatalytic performance in a multi-step electrochemical process.^{32, 33} For example, Wei *et al.*³⁴ reported that the reconstituted Cu₄ clusters supported on CeO₂ demonstrate good catalytic performance in electrocatalytic urea synthesis, yielding an average urea yield rate of 52.84 mmol h⁻¹ g_{cat.}⁻¹ at -1.6 V *versus* reversible hydrogen electrode (RHE). Liu *et al.*³⁵ showed that the Cu clusters supported on quasi-amorphous cobalt sulfide can serve as efficient electrocatalysts for water splitting. Additionally, Ling *et al.*³⁶ constructed a dual Cu-Fe site by anchoring Cu₅ clusters on the surface of FeS₂, effectively boosting the H₂O₂ activation. Furthermore, Xu and coworkers³⁷ discovered that carbon-supported Cu clusters can electrochemically

convert CO₂ to C₂H₅OH with a high Faradaic efficiency of 91% at -0.7 V and a low onset potential of -0.4 V.

Considering the unique structures and great potential of SMCs in electrocatalysis, we are highly intrigued by their applications in synthesizing C₂H₄ from CO₂ER. In this regards, Hori *et al.* reported that the formation of C₂H₄ product is sensitively dependent on the surface orientation of the Cu electrode: Cu(100) is especially beneficial to C₂H₄ generation.³⁸ Further theoretical studies revealed that the chemisorbed CO dimer (*C₂O₂) is the key intermediate for the C–C coupling on Cu(100), which is primarily attributed to its unique square symmetry structure. Specially, *C₂O₂ is a geometry-sensitive adsorbate, and only square-like sites can lead to suitable *C₂O₂ adsorption configuration with low kinetic barrier. Besides, the amount of charge transfer from the Cu(100) surface (square symmetry formed by four atoms) to the adsorbed *C₂O₂ species is larger than that of the hexagonal-symmetry sites formed by three atoms, which also facilitates the C–C coupling at the square-symmetry surface sites with a low kinetic barrier.^{39,40}

Inspired by these above innovative studies on the remarkable performance of Cu-based square-like sites for the CO₂-to-C₂H₄ process, an interesting question arises: can a Cu cluster supported by a suitable substrate, possessing a square-like structure akin to the Cu(100) catalyst, be effectively employed for the reduction of CO₂ into C₂H₄? To address this issue, herein, we carried out a systematic density functional theory (DFT) study on the design of Cu-based clusters anchored on defective molybdenum disulfide (MoS₂) monolayer with sulfur (S) vacancies as effective and highly selective catalysts

for the reduction of CO₂ to C₂H₄. Notably, S vacancies can naturally occur during the preparation of MoS₂ monolayer,⁴¹⁻⁴³ and have been widely employed as substrates for anchoring various SCMs, such as Cu,⁴⁴⁻⁴⁷ Ag,⁴⁸ and Pt clusters.^{49,50} Especially, MoS₂-based materials have been proposed as efficient catalysts for CO₂ electrochemical reduction, including the anchored SACs and the exposed edges, in which some C₁ products can be obtained, such as CO, CH₄, and CH₃OH.⁵¹⁻⁵⁶ To the best of our knowledge, however, there are few reports on generating multicarbon products on these MoS₂-based catalysts.^{57,58}

Our computational results demonstrated that the Cu₅ cluster anchored on an S vacancy site (Cu₅@MoS₂) features a square-like structure: one Cu atom is embedded within the S vacancy, while the remaining Cu atoms form a square-like Cu-based island. Moreover, Cu₅@MoS₂ has excellent structural stability and high electrical conductivity. The square-like sites of Cu₅@MoS₂ facilitate the C–C coupling reaction between two adsorbed *CO species to form a *C₂O₂ intermediate with a low kinetic barrier of 0.56 eV. Importantly, the *C₂O₂ intermediate can be easily reduced to C₂H₄ with high selectivity, while effectively suppressing competing side reactions. The catalytic activity of Cu₅@MoS₂ is reflected by its rather lower limiting potential of –0.32 V, which is even less negative than the state-of-the-art Cu(100) benchmark (–0.61 V). More importantly, the activity of Cu₅@MoS₂ towards the CO₂-to-C₂H₄ conversion can be further enhanced by the alkaline conditions according to the constant-potential method. Therefore, Cu₅@MoS₂ demonstrates compelling electrocatalytic properties, including high activity, high selectivity, and low cost, for the reduction of CO₂ to C₂H₄.

2. Computational Methods

All spin-polarized DFT computations were performed by using the Vienna Ab Initio Simulation Package (VASP)^{59, 60} with the ion-electron interactions represented by the projector augmented wave (PAW) method.^{61, 62} The Perdew-Burke-Ernzerhof (PBE) functional⁶³ within the generalized gradient approximation (GGA) and a cutoff energy of 550 eV for the plane-wave basis set were employed. To ascertain the accuracy of computations of the PBE functional, we repeated related computations for CO₂ER on Cu₅@MoS₂ by using the more reliable revised Perdew-Burke-Ernzerhof (rPBE) functional,⁶⁴ and the detailed results were shown in Fig. S1. Small differences between the results of PBE and rPBE functionals guarantee the validity of the conclusions in this work. The Grimme's scheme (DFT+D3)⁶⁵ was adopted to treat the van der Waals (vdW) interactions between the adopted species and Cu₅@MoS₂. The convergence criterion for the geometrical optimization was set to 0.02 eV/Å in residual force and 10⁻⁵ eV in energy, respectively. The partial charge transfer was computed based on the Bader charge analysis.⁶⁶

The Cu₅@MoS₂ system was constructed by anchoring a Cu₅ cluster on a 4 × 4 × 1 MoS₂ supercell with an S vacancy. The supercell consists of 16 Mo atoms, 31 S atoms, and 5 Cu atoms. To prevent interactions between periodic images, a vacuum space of 20 Å was included in the system. The Brillouin zone in the reciprocal space of Cu₅@MoS₂ was sampled using a Monkhorst–Pack *k*-point mesh with a 3 × 3 × 1 *k*-point grid. The freestanding Cu₅ cluster was computed in a 10 × 10 × 10 Å³ unit cell with 5 × 5 × 5 Monkhorst–Pack *k*-point meshes.

To assess the thermal stability of Cu₅@MoS₂, ab initio molecular dynamics (AIMD) simulations were performed in the canonical ensemble (NVT) with the Nose-Hoover thermostat⁶⁷ at 300K. The simulations were carried out for 20 ps with a time step of 2 fs. The climbing image nudged elastic band (CI-NEB)⁶⁸ was employed to determine the minimum energy pathway for the C-C coupling and compute the kinetic barrier.

The binding energy (E_b) of the Cu₅ cluster on the defective MoS₂ monolayer was computed by: $E_b = E(\text{Cu}_5@\text{MoS}_2) - E(\text{Cu}_5) - E(\text{MoS}_2)$, where $E(\text{Cu}_5@\text{MoS}_2)$, $E(\text{Cu}_5)$, $E(\text{MoS}_2)$ represent the total energies of the Cu₅ cluster supported on the MoS₂ monolayer, the isolated Cu₅ cluster, and the bare MoS₂ monolayer with an S vacancy, respectively. According to this definition, a more negative E_b value suggests a stronger interaction.

To explore the catalytic activity of Cu₅@MoS₂ toward CO₂ER, the computational electrode model (CHE) method^{69,70} was employed to compute the free energy diagrams and the limiting potentials of the CO₂-to-C₂H₄ process. The free energy change (ΔG) of each elementary step in CO₂ER can be obtained by the formula: $\Delta G = \Delta E + \Delta ZPE - T\Delta S + eU$, where ΔE is the reaction energy of reactant and product species adsorbed on the catalyst directly obtained from DFT computations; ΔZPE and ΔS represent the differences in zero-point energy and entropy, respectively, between the adsorbed species and the gas phase molecules at 298.15 K, which can be calculated from the vibrational frequencies. U was the applied potential. According to the obtained free energy change of each elementary step, the limiting potential (U_L) was further computed as follows: $U_L = -\max(\Delta G_1, \Delta G_2, \Delta G_3, \Delta G_4, \dots, \Delta G_i)/e$.

To elucidate the reaction mechanism under different electrode potentials, we carried out computations using the constant-potential method, in which the excess charge per unit cell (Δn) ranging from $-2.0 e^-$ to $+2.0 e^-$ with a step size of $0.5 e^-$ was incrementally introduced. A reference value of 4.6 eV was adopted for the standard hydrogen electrode (SHE). The potential-dependent energy can be calculated by: $E = E_{DFT} - \Delta n(V_{sol} + \varphi_q)/e$, where E_{DFT} is the DFT-calculated energy, V_{sol} is the electrostatic potential of the bulk electrolyte, and $-\varphi_q$ is the work function of the charged system. The relation between φ_q and the corresponding electrode potential referenced to the standard hydrogen electrode (SHE) scale is $U_q(U/SHE) = -4.6V - \varphi_q/e$. The $E-U_q$ quadratic form can be written as: $E(U_q) = -\frac{1}{2}C(U_q - U_0)^2 + E_0$, where U_0 , C , and E_0 are the fitted values of the potential of zero charge (PZC), the capacitance of the corresponding system, and the energy of the system at the PZC, respectively. The fixed potential, referenced to the standard hydrogen electrode (SHE) scale, varies with the pH value. The relationship between the SHE potential (U_{SHE}) and the reversible hydrogen electrode (RHE) potential (U_{RHE}) is given by $U_{RHE} = U_{SHE} + 0.0592 \times \text{pH}$. This equation enables the determination of the RHE potential based on the pH value.

3. Results and Discussion

3.1. Geometric Structure, Stability, and Electronic Property.

First, we examined the structure and stability of the adsorbed Cu_5 cluster on the S vacancy of the MoS_2 substrate. For the freestanding Cu_5 cluster, both planar and three-dimensional (3D) structures were considered (Fig. S2a), as they are the two lowest

energy isomers of the Cu_5 cluster.⁷¹ Then, the two Cu_5 clusters were positioned on various sites of the defective MoS_2 monolayer, including the S vacancy site, the Mo site's top, and the hollow site within the Mo_3S_3 ring.

As expected, both of the two Cu_5 clusters exhibit a preference for binding to the S vacancy after full atomic relaxation (Fig. S2b). Interestingly, the binding of the 3D Cu_5 cluster to the defective MoS_2 monolayer is much stronger than that of the planar Cu_5 cluster, as evidenced by their respective E_b values of -5.07 eV vs -4.23 eV. These values are more negative than the cohesive energy of the bulk Cu materials (-3.86 eV), highlighting the exceptional capability of the S vacancy site within the defective MoS_2 substrate to firmly immobilize Cu_5 clusters. Consequently, the subsequent discussion will primarily focus on the stability and properties of the 3D Cu_5 cluster supported on the defective MoS_2 substrate.

Noteworthy, this configuration allows for the formation of a reverse pentahedral Cu_5 cluster (Fig. 1a). In this arrangement, one Cu atom is fully embedded into the framework of MoS_2 monolayer, occupying the position previously occupied by the removed S atom, and forming three Cu-Mo bonds with lengths of 2.50 Å. Meanwhile, the remaining four Cu atoms are positioned outward from the MoS_2 surface, forming a square-like Cu island with Cu-Cu lengths of about 2.49 Å, with the bottom Cu atom binding to the island with a length of 2.32 Å. The square-symmetry surface sites of the Cu_5 cluster result in the particular “double-bridge state” within an identical coordination environment. This configuration is advantageous for the parallel attack and simultaneous activation of two CO_2 molecules. In addition, the appropriate distance of

2.49 Å between adjacent Cu-Cu bridge sites may promote the C-C coupling of carbon-containing intermediates. Obviously, the structural feature of the anchored Cu₅ cluster bear a striking resemblance to that of the Cu(100) slab⁷²⁻⁷⁴ and meet the intrinsic requirements for the electroreduction of CO₂ to C₂H₄.

Furthermore, the stability of Cu₅@MoS₂ was evaluated through AIMD simulations at 300 K for 20 ps (Fig. S3), from which we found that the structure of this catalyst can be well maintained, suggesting that the 3D Cu₅ cluster can be firmly anchored to the S-vacancy of the MoS₂ substrate to ensure its high stability. In addition, we examined the electrochemical stability of Cu₅@MoS₂ by exploring whether its bare surfaces would be covered by *O/*OH species in an aqueous solution under operation. To address this, a surface Pourbaix diagram was constructed, which represents the most stable surface structures under realistic conditions.^{75, 76} The results revealed that at an electrode potential of 0 V, the Cu₅@MoS₂ surface is predominantly covered by *OH species across all pH values. However, upon the application of electrode potential, the *OH species will be hydrogenated to H₂O. Importantly, at pH=0, the minimum potential required to remove the surface *OH species (U_R) is -0.10 V (Fig. 1b), which is less negative than the limiting potential of CO₂ER (-0.32 V as discussed later). Besides, we also computed the dissolution potential (U_{diss} , more details are given in Supporting Information) of the Cu active site in Cu₅/MoS₂ catalyst at the operating potential of the cathode (*i.e.*, negative overpotential, $-\eta$). Remarkably, the U_{diss} of the Cu active site within the anchored Cu₅ cluster (-0.04 V) is significantly less negative than the ($-\eta$) value of CO₂-to-C₂H₄ on this catalyst (η = 0.38 V, see Supporting Information).⁷⁷

Consequently, the $\text{Cu}_5@ \text{MoS}_2$ system exhibits excellent electrochemical stability against surface oxidation and can withstand the practical reaction environments of CO_2ER under working conditions. Note that the successful synthesis of Cu clusters on MoS_2 -based substrates with point defects has been experimentally demonstrated.⁴⁴⁻⁴⁷ These experimental findings greatly inspired us further to explore the catalytic performance of such systems in CO_2ER .

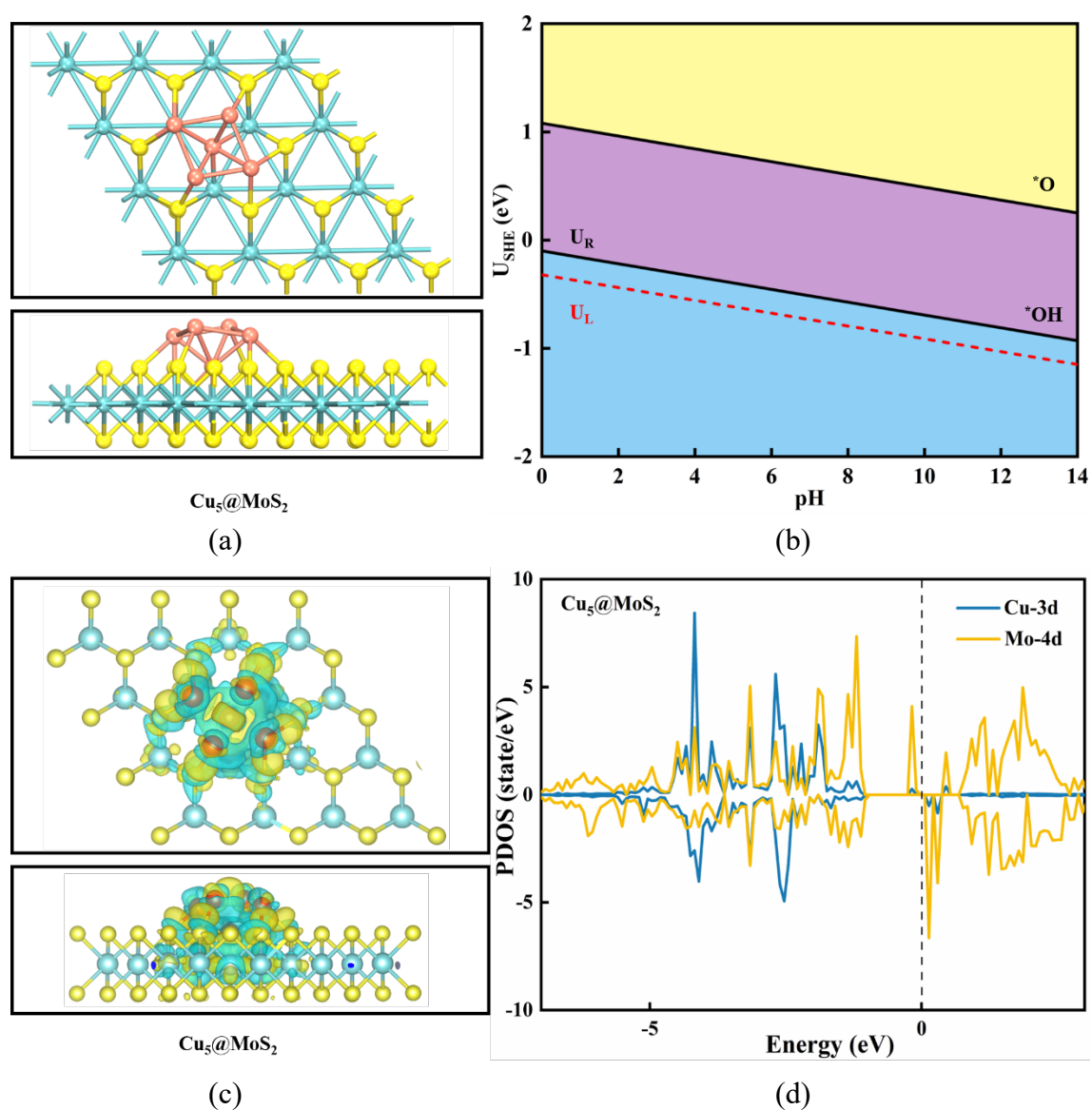


Fig. 1. a) Optimized structure of $\text{Cu}_5@ \text{MoS}_2$ from both the top and side views. b) Surface Pourbaix diagram of $\text{Cu}_5@ \text{MoS}_2$. The thermodynamically stable states of the

surface under SHE and pH values are highlighted by yellow regions for *O and pink regions for *OH. The red dashed line represents the limiting potential of CO₂ER. c) Differential charge density plot of Cu₅@MoS₂, with yellow representing electron accumulation and cyan denoting electron depletion. The isosurface value is set to be 0.005 e Å⁻³. d) Spin-polarized partial density of states (PDOS) of the 3d-orbitals of the bottom Cu atom and the 4d-orbitals of the adjacent Mo atoms in the Cu₅@MoS₂ system.

To gain deep insights into the strong interaction of the Cu₅ cluster on the S-vacancy site of the MoS₂ monolayer, we examined the charge transfer and the orbital hybridization between them. As shown in Fig. 1c, we observed partial oxidation of the Cu atom that is captured by the S vacancy site, leading to the formation of three strong-polarized Cu-Mo bonds through the hybridization of Cu-3d and Mo-4d orbitals (Fig. 1d). Moreover, the top four Cu atoms in the adsorbed Cu₅ cluster carry a nearly identical positive charge of 0.22 |e|, indicating their uniform coordination environments and confirming the square-symmetry feature. This square-symmetry is known to facilitate the transfer of more electrons to the CO₂ER intermediates. In addition, according to the computed band structure, this pristine MoS₂ substrate exhibits a semiconducting characteristic with a band gap of 1.12 eV (Fig. S4a). Upon the adsorption of the Cu₅ cluster adsorption, however, some impurity states are introduced into the band structure (Fig. S4b), greatly reducing the band gap to 0.11 eV and thus resulting in an enhanced electrical conductivity, which is beneficial for the process of CO₂ER.

3.2. CO₂ER Performance on Cu₅/MoS₂.

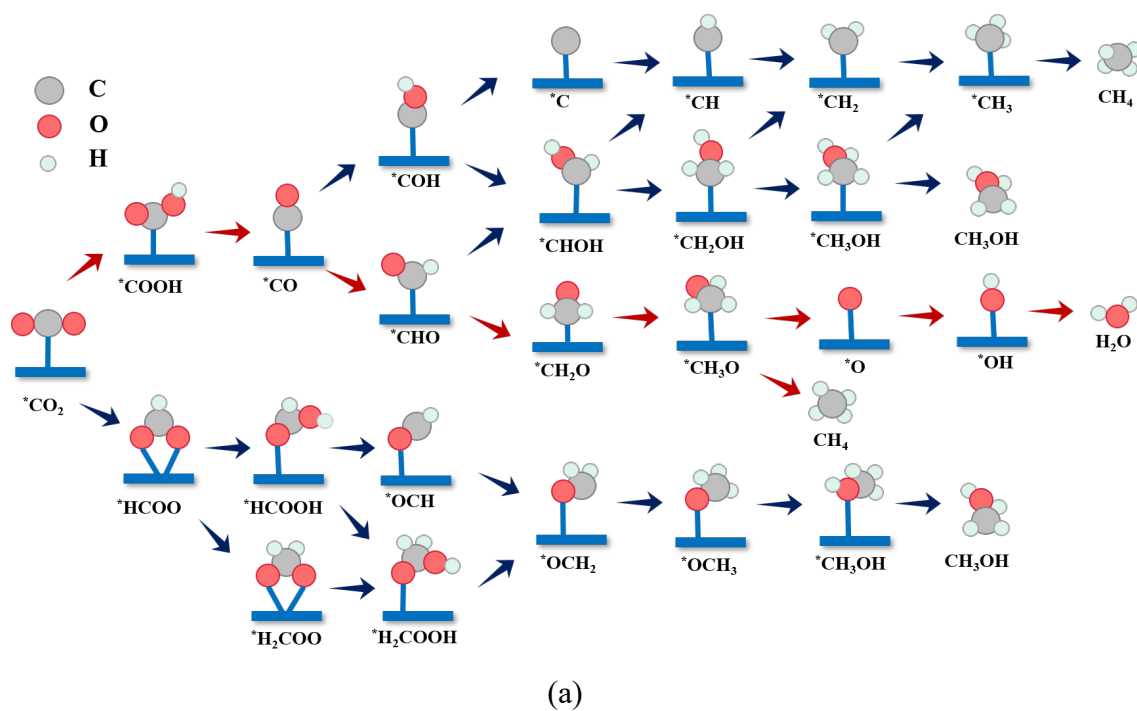
Efficient CO₂ electroreduction (CO₂ER) relies on successfully activating CO₂ on the catalyst surface. After fully structural relaxation, we found that the C atom of CO₂ is preferable be adsorbed on the Cu-Cu bridge site with the lengths of 2.06 Å, while its two O atoms bind with the Cu top site with the lengths of 2.11 Å. Compared with the linear structure of the free CO₂ molecule, the adsorbed *CO₂ experiences a C-O bond length elongation of 0.06, and a bending of the O-C-O angle is by 40° (Fig. S5a). These structural changes indicate the sufficient activation of *CO₂ on the Cu₅/MoS₂ system. Notably, the explicit solvent can further increase the *CO₂ adsorption strength by about 0.45 eV (Fig. S5b), while a small change (≤ 0.05 V) can be observed for the computed limiting potential by different solvent effects (Table S1), which has been widely regarded as an criterion to estimate the catalytic activity of CO₂ER on a given catalyst. It is easily understood that the CO₂ activation originates from substantial charge transfer from the Cu-3d orbitals into the CO₂-2 π^* orbitals (0.54 |e|) and strong hybridizations between the Cu-3d orbitals and the C/O-2p orbitals (Fig. S5c). This substantial charge transfer and orbital hybridization contribute to the effective capture and activation of CO₂ on Cu₅@MoS₂, which will likely facilitate its subsequent reduction.

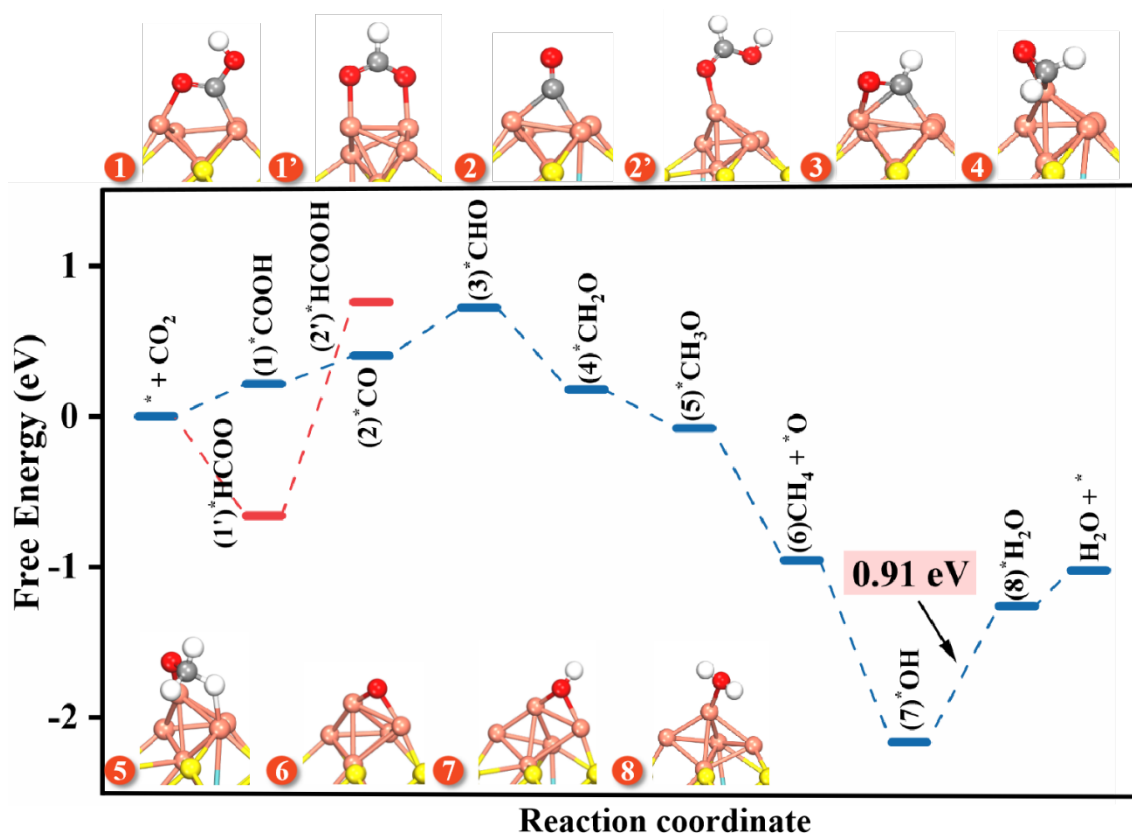
Having established the sufficient activation of the CO₂ molecule, we evaluated the catalytic activity and the product distribution of CO₂ER on the Cu₅@MoS₂ catalyst. In order to reveal the reaction mechanisms, we employed the CHE method to identify the reaction pathway with the lowest positive free energy change between any two elementary steps, which corresponds to the most favorable reaction pathway. Then, the

applied voltage required for the entire reaction to become exergonic, known as the limiting potential (U_L), was determined.

3.2.1. CO₂ER leading to C₁ products.

By considering various possible reaction pathways (Fig. 2a), we thoroughly examined the feasibility of CO₂ electroreduction to C₁ products on the Cu₅@MoS₂ catalyst and identified the most favorable reaction pathway (Fig. 2b).





(b)

Fig. 2. (a) Possible reaction pathways considered for CO₂ER leading to C₁ products. (b) Free energy diagram for CO₂ER to CH₄ product on Cu₅@MoS₂ surface, along with the corresponding configurations of the reaction intermediates.

Based on the computed free energy changes of all elementary steps along the lowest-energy pathway, we revealed the following sequence of reactions. Firstly, one O atom of CO₂ is hydrogenated to generate ^{*}COOH species with an uphill free energy of 0.22 eV. Note that this energy barrier is lower than that observed on the Cu(211) surface (0.41 eV)⁷⁸ and the Cu (100) surface (0.52 eV)²⁴. Subsequently, the ^{*}COOH intermediate reacts with a second (H⁺ + e⁻) pair, resulting in the formation of (^{*}CO + H₂O). Remarkably, the ^{*}CO formation is slightly endothermic by 0.18 eV, which is significantly lower than that of the competitive ^{*}HCOOH formation (ΔG = 0.54 eV).

Moreover, due to the strong adsorption strength (-0.96 eV), the formed $^*\text{CO}$ undergoes further hydrogenation to generate the $^*\text{CHO}$ species, and this step only requires a small energy input of 0.32 eV, which is lower by 0.56 eV than that of the competing $^*\text{COH}$ formation. In the following step, the ($\text{H}^+ + \text{e}^-$) pair continually attacks the C site of $^*\text{CHO}$, leading to the formation of $^*\text{CH}_2\text{O}$ and $^*\text{CH}_3\text{O}$ after two consecutive hydrogenation steps. Importantly, these reactions occur downhill in the free energy profile by 0.54 and 0.26 eV, respectively. Next, the hydrogenation of $^*\text{CH}_3\text{O}$ intermediate induces the C–O bond breaking, resulting in the release of the CH_4 product. This step is exothermic by 0.88 eV in the free energy diagram. Meanwhile, the remaining O atom on the Cu–Cu bridge with a length of 1.78 Å undergoes further hydrogenation to form $^*\text{OH}$ with the ΔG of -1.21 eV, followed by its subsequent hydrogenation to generate the second H_2O . However, this step of $^*\text{OH} \rightarrow ^*\text{H}_2\text{O}$ is endothermic by 0.91 eV due to the strong $^*\text{OH}$ adsorption on $\text{Cu}_5@/\text{MoS}_2$ (-4.76 eV).

Overall, in the CO_2 -to- CH_4 process, the $^*\text{OH}$ hydrogenation is identified as the potential-determining step (PDS) due to its maximum ΔG value of 0.91 V (Fig. 2), corresponding to the U_L of -0.91 V, which is even more negative than that observed on the Cu(211) slab (-0.74 V)⁷⁰ and the competitive HER process (-0.86 V). Therefore, the formation of CH_4 as a product is unlikely to be achieved on the $\text{Cu}_5@/\text{MoS}_2$ surface. Instead, we expect $^*\text{CO}$ species to be the main product at low potential due to its remarkable binding strength with this catalyst (-0.96 eV).

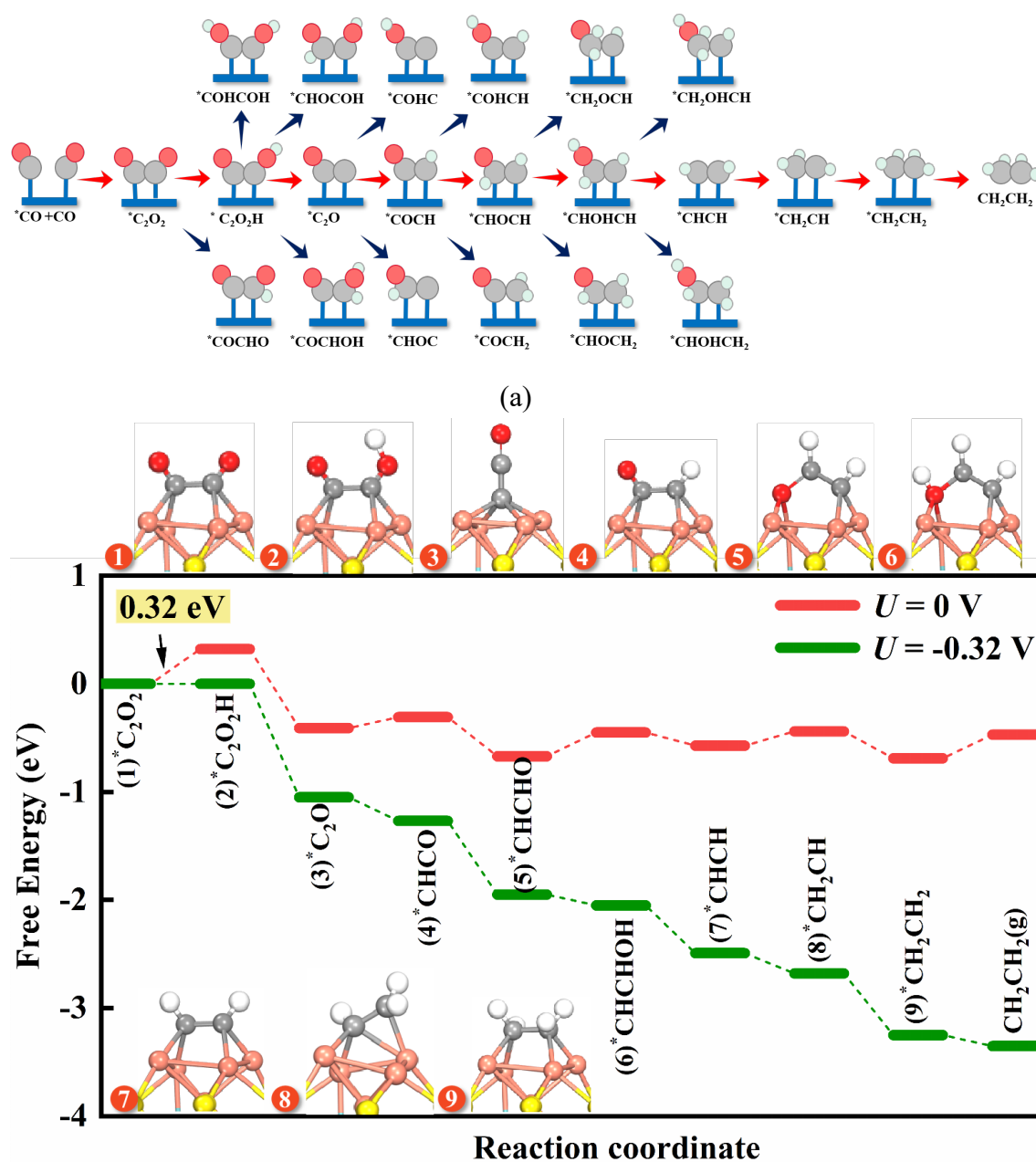
3.2.2. CO_2 ER leading to C_2 products.

Due to the unique “double-bridged” active sites in the $\text{Cu}_5@\text{MoS}_2$ system, after $^*\text{CO}$ is adsorbed on a Cu-Cu bridge site, the other Cu-Cu bridge site can continue to activate and convert the CO_2 molecule. Interestingly, the hydrogenation free energies of CO_2 and $^*\text{COOH}$ are greatly reduced with the increase of CO_2 , calculated to be 0.02 and -0.48 eV, respectively (Fig. S6a). As a result, two separate chemisorbed $^*\text{CO}$ species on the two opposing bridge sites of $\text{Cu}_5@\text{MoS}_2$ are formed. Previous studies^{24, 65} have indicated that the C-C coupling step *via* $^*\text{CO}$ dimerization to $^*\text{C}_2\text{O}_2$ intermediate is crucial for C_2H_4 generation on Cu(100) surface during CO_2ER . Therefore, we explored the potential for coupling the two $^*\text{CO}$ species on $\text{Cu}_5@\text{MoS}_2$. Excitingly, the kinetic barrier for this coupling reaction is only 0.56 eV (Fig. S6b), even lower than that of on Cu(100) surface (0.82 eV),²⁹ highlighting the unique advantage of Cu-based square-like sites in promoting C-C coupling.

In addition to $^*\text{CO}$ dimerization, we also considered two other common C-C coupling steps, namely, ($^*\text{CHO} + ^*\text{CO}$) and ($^*\text{CHO} + ^*\text{CHO}$) couplings, for comparison. However, as shown in Fig. S7, the computed kinetic barriers for these two coupling reactions, 1.72 and 0.99 eV, respectively, are significantly higher than that of the CO dimerization (0.56 eV). Thus, the C-C coupling between $^*\text{CO}$ species is kinetically favorable and feasible on $\text{Cu}_5@\text{MoS}_2$. A similar phenomenon was also observed on Cu(100) slab.²⁹

We proceeded to investigate the thermodynamics of the subsequent hydrogenation steps of the $^*\text{C}_2\text{O}_2$ intermediate to form C_2 products, following the successful C-C coupling through $^*\text{CO}$ dimerization. In this process, various reaction pathways were

considered, including O-H bond formation, C-H bond formation, and C-OH bond breaking processes (Fig. 3a). By determining the most stable structure for each intermediate, we obtained the free energy diagram along the most energetically favorable pathway for CO₂ER to C₂ products, as depicted in Fig. 3b. For comparison, we summarized the free energy changes along other less favorable pathways in Table S2.



(b)

Fig. 3. (a) Possible reaction pathways considered for CO₂ER to C₂ products. (b) Free energy diagram for C₂H₄ generation along the most favorable pathway, along with the corresponding configurations of the reaction intermediates.

Our results showed that the (H⁺ + e⁻) pairs preferentially attack one of the oxygen atom of *C₂O₂, leading to the formation of *C₂O₂H, and then continuously approaches this oxygen atom, resulting in the generation of *C₂O and the release of a H₂O molecule. Remarkably, the formation of *C₂O₂H is slightly uphill by 0.32 eV, whereas *C₂O formation is downhill by 0.73 eV in the free energy profile. Note that the *C₂O species is vertically adsorbed on the fourfold hollow site of the Cu₅@MoS₂ system *via* the C-end pattern with a length of about 2.00 Å.

In the following steps, the hydrogenation of *C₂O preferentially proceeds along the *C₂O → *CHCO → *CHCHO → *CHCHOH pathways, with ΔG values of 0.10, -0.36, and 0.22 eV, respectively. Once *CHCHOH is formed, the subsequent pathway bifurcates into two routes: C₂H₄-formation and C₂H₅OH-formation. Interestingly, we found that the formation of *CHCH intermediate, which can be regarded as the precursor of C₂H₄ product, is more favorable than *CH₂CHOH and *CHCH₂OH, with the ΔG value lower by 0.25 and 0.49 eV, respectively. This ΔG difference suggests that C₂H₄ is likely the main product of CO₂ER on the Cu₅@MoS₂ system. After the formation of *CHCH species, the production of C₂H₄ proceeds smoothly through two successive hydrogenation steps, with corresponding free energy changes of 0.13 and -0.25 eV, respectively. Finally, the formed C₂H₄ molecule is released from the

Cu₅@MoS₂ surface with a low energy input of 0.22 eV, allowing the regeneration of the catalyst for subsequent catalytic cycles.

Now, a comprehensive reaction pathway for CO₂ER to C₂H₄ on the Cu₅@MoS₂ catalyst surface can be summarized as follows: CO₂ + * → *COOH → *CO → *C₂O₂ → *C₂O₂H → *C₂O → *CHCO → *CHCHO → *CHCHOH → *CHCH → *CH₂CH → *CH₂CH₂ → CH₂CH₂ + *. In this pathway, the hydrogenation of *C₂O₂ is the PDS with a free energy change of 0.32 eV. According to the CHE model, the smallest applied potential of -0.32 V required to make all elementary reactions exergonic, that is, the limiting potential is -0.32 V (Fig. 3), which is less negative than the Cu(100) benchmark (-0.61 V),²⁴ suggesting the higher catalytic activity of our designed Cu₅@MoS₂ catalyst in promoting the CO₂ER process and facilitating C₂H₄ generation. Furthermore, we computed the activation barriers to simulate the mechanism of C₂H₄ formation from a kinetic perspective by using one water assisted hydrogen shuttling model, which has been extensively adopted to compute the barriers of electrochemical CO₂ reduction⁷⁹⁻⁸¹ We found that the largest activation barrier of 0.73 eV locates at the protonation of *C₂O₂ (Fig. S8), which is higher than than of *CO dimerization (0.56 eV), but is lower than 0.75 eV that corresponds to a fast electrochemical process.⁸² Thus, Cu₅@MoS₂ is facile for the electrochemical reduction of CO₂ to C₂H₄ product kinetically.

In addition, considering that the CO₂ER takes place in aqueous solutions, we also evaluated the solvent effect on the catalytic activity using the implicit solvation model implemented in VASPsol.⁸³ It can be clearly seen from Fig. S9 that the PDS with

solvent effect still locates at the *C_2O_2 hydrogenation with the limiting potential of -0.30 V, which is comparable to that of without solvent effect of -0.32 V, indicating that the solvent environment is not an obstacle to impair the excellent catalytic activity of $Cu_5@MoS_2$ towards C_2H_4 synthesis from the CO_2ER .

The selectivity of this catalyst toward C_2H_4 production is also noteworthy. For this regard, we examined two major competing reactions, namely the hydrogen evolution reaction (HER) and the formation of C_2H_5OH on the $Cu_5@MoS_2$ surface. For HER, the energy input required for H_2 release is significantly higher (0.86 eV) compared with that for C_2H_4 synthesis (0.32 eV). Moreover, the binding strength of the key *COOH intermediate on the $Cu_5@MoS_2$ catalyst is much stronger (-2.79 eV) than that of *H species (-1.09 eV), suggesting a preference for the adsorption of *COOH species on the active site. These findings indicate the excellent suppression effect of the Cu active sites within the anchored Cu_5 cluster on the competitive HER.

The C_2H_4 *versus* C_2H_5OH selectivity highly depends on the adsorption strength of *OH on the catalyst surface. The square-like sites of the anchored Cu_5 cluster exhibit a relatively strong *OH binding, making it more difficult for Cu–O bond breaking compared to O–C bond breaking. As a result, the C_2H_4 production is thermodynamically more favorable than the C_2H_5OH production by at least 0.25 eV (Table S2). The distribution of the two products can be further evaluated by the thermodynamic formula $\exp[-(\Delta G)/(RT)]$. In this equation, ΔG is the free energy difference for the formation of ($^*CHCH + H_2O$) and (*CH_2CHOH); here $\Delta G = 0.25$ eV at $T = 298$ K. Thus, the $C_2H_4:C_2H_5OH$ molar ratio is computed to be about $1.68 \times 10^4:1$

at ambient temperature, suggesting a rather high C₂H₄ selectivity, thanks to its unique square-like active sites.

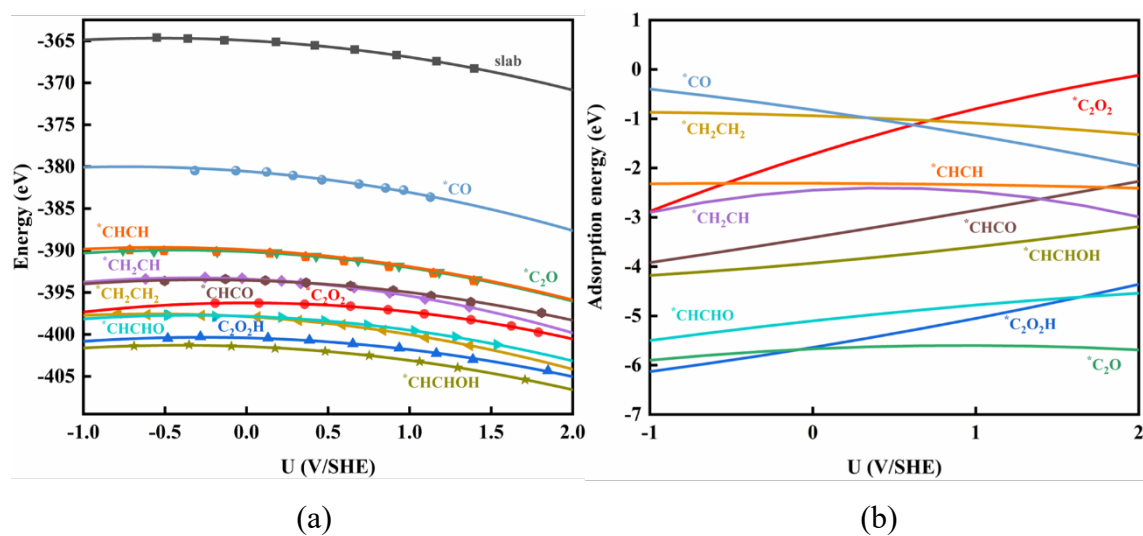
3.3. pH-dependent CO₂ER activity.

Although the CHE model has predicted the superior catalytic performance of Cu₅@MoS₂ for CO₂ER to C₂H₄ and also provided insights into the reaction mechanism, it fails to capture the pH-dependent activity due to the cancellation of pH and electrode potential corrections.⁸⁴⁻⁸⁸ Actually, many experimental studies demonstrated that CO₂ER activity for C₂H₄ production on Cu-based catalysts is generally higher under alkaline conditions compared to acidic conditions.⁵ Therefore, understanding the pH-dependent activity is crucial in CO₂ electroreduction. Recently, Duan *et al.* successfully addressed this issue by utilizing their constant-potential method (CPM), which accounts for solvent and constant-potential effects in electrocatalysis to simulate a more realistic environment.⁸⁹⁻⁹³

To examine the pH impact on the CO₂ER activity of Cu₅@MoS₂, we employed the CPM combined with the implicit solvent model. By analyzing the energetics of CO₂ER, we obtained the computed total energies of bare Cu₅@MoS₂ surface and the adsorbed reaction intermediates along the most favorable pathway of the CO₂-to-C₂H₄ process as a function of the applied electrode potential (Fig. 4a). Encouragingly, all energy-potential points align well with a quadratic relationship, and the specific fitted data are listed in Table S3. Furthermore, we compiled the computed E_{ads} values of these C-based reaction intermediates with respect to the applied potential (in Fig. 4b).

Additionally, we plotted the pH-dependent and potential-dependent contour

illustrating the adsorption energies of *C_2O_2 on $Cu_5@MoS_2$ (Fig. 4c), as this intermediate is closely related to the PDS. Our simulations showed that the adsorption strength of *C_2O_2 on the $Cu_5@MoS_2$ catalyst increases as the pH increases or the applied potential decreases. For example, at pH = 1, the E_{ads} of *C_2O_2 is -1.78 eV, while at pH = 13, it rises to -2.59 eV, suggesting that the alkaline conditions enhance the activation of *C_2O_2 . Therefore, the CO_2ER activity of $Cu_5@MoS_2$ is indeed pH-dependent. Especially, we found that this catalyst exhibits the highest catalytic activity at pH = 13 (Fig. S10), corresponding to an exceptionally low limiting potential of -0.25 V vs reverse hydrogen electrode (RHE) (Fig. 4d). Notably, due to the strong *C_2O_2 adsorption at pH = 13, the PDS turns into the hydrogenation of *CHCHO to *CHCHOH .



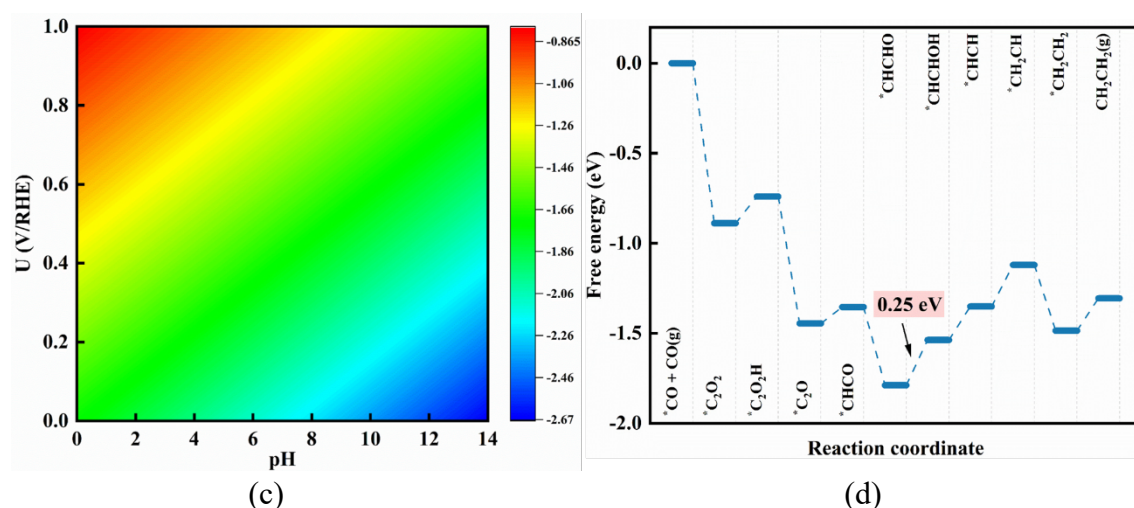


Fig. 4. The computed total energies of the $\text{Cu}_5@MoS_2$ catalyst and the corresponding reaction intermediates as a function of the applied electrode potential. (b) Adsorption energies of various C-based reaction intermediates as a function of the applied electrode potential. (c) pH-dependent and potential-dependent contour plot of adsorption energies of *C_2O_2 on $\text{Cu}_5@MoS_2$ surface. (d) The free energy profile for CO_2 -to- C_2H_4 conversion on $\text{Cu}_5@MoS_2$ at $pH = 13$.

3.4. Square-Like Active Sites of $\text{Cu}_5@MoS_2$ vs. Anchored Cu_n Clusters in CO_2 Electroreduction

To highlight the significance of the square-like active sites of $\text{Cu}_5@MoS_2$ in facilitating C_2H_4 production, we also examined the catalytic performance of other anchored Cu_n clusters ($n = 1, 2, 3, 4,$ and 6) for C–C coupling in CO_2ER . As expected, for a single Cu atom, the C–C coupling is not feasible due to the absence of sufficient active sites. For other Cu clusters, we found that the coupling between two adsorbed CO species is unstable, resulting in their spontaneous optimization into two isolated CO species after full structural relaxation (Fig. S11a).

Furthermore, we computed the kinetic barriers (E_{barrier}) for the C-C coupling *via* the “carbene” mechanism, focusing on the coupling between CO^* and CHO^* as a representative case. We found the coupling of CO^* with CHO^* on these Cu clusters is not facile, because their E_{barrier} values are larger than 0.75 eV (1.00 to 1.53 eV, Fig. S11b). These results further underscore the distinct advantages of the square-like active sites in $\text{Cu}_5@ \text{MoS}_2$ for boosting the C-C coupling.

4. Conclusions

In summary, by means of comprehensive DFT computations, we designed a promising CO_2ER catalyst for C_2H_4 synthesis by anchoring a 3D Cu_5 cluster on a defective MoS_2 monolayer. The S monovacancy enables the formation of a unique square-like active site, which can effectively promote the C-C coupling between two $^*\text{CO}$ species with a low kinetic barrier of 0.56 eV. Moreover, the resulting $^*\text{C}_2\text{O}_2$ intermediate can be easily hydrogenated to C_2H_4 product with a lower limiting potential (-0.32 V) than the $\text{Cu}(100)$ benchmark. Importantly, the $\text{Cu}_5@ \text{MoS}_2$ surface effectively suppresses side reactions such as HER and the $\text{CH}_4/\text{C}_2\text{H}_5\text{OH}$ formation, ensuring high selectivity toward C_2H_4 production. Notably, the conversion of CO_2 to C_2H_4 is pH-dependent, with the highest catalytic activity observed at pH 13, accompanied by a remarkably low limiting potential of -0.25 V. Our findings not only propose a promising catalyst for C_2H_4 synthesis via CO_2ER , but also offer a feasible strategy to design highly-efficient catalysts using anchored sub-nano clusters. This work is expected to inspire more experimental and theoretical studies to explore the potential

applications of such catalysts in various other electrochemical reactions.

NOTES

The authors declare no competing financial interest.

ACKNOWLEDGEMENT

This work was financially supported in China by the Natural Science Foundation of Heilongjiang Province of China (TD2020B001) and the Natural Science Funds for Distinguished Young Scholar of Heilongjiang Province (No. JC2018004), and in the USA by the Department of Energy, Office of Basic Energy Sciences under Award Number DE-SC0023418.

References

1. J. Qiao, Y. Liu, F. Hong and J. Zhang, *Chem. Soc. Rev.*, 2014, **43**, 631-675.
2. Y. Y. Birdja, E. Pérez-Gallent, M. C. Figueiredo, A. J. Göttle, F. Calle-Vallejo and M. T. M. Koper, *Nat. Energy*, 2019, **4**, 732-745.
3. J.-J. Wang, X.-P. Li, B.-F. Cui, Z. Zhang, X.-F. Hu, J. Ding, Y.-D. Deng, X.-P. Han and W.-B. Hu, *Rare Metals*, 2021, **40**, 3019-3037.
4. A. N. El Aisnada, M. Miyauchi, M. Liu and A. Yamaguchi, *Mater. Reports: Energy*, 2023, 100190.
5. X. Chen, Y. Zhao, J. Han and Y. Bu, *ChemPlusChem*, 2023, **88**, e202200370.
6. H. S. Jeon, S. Kunze, F. Scholten and B. Roldan Cuenya, *ACS Catal.*, 2018, **8**, 531-535.

7. J.-J. Li and Z.-C. Zhang, *Rare Metals*, 2022, **41**, 723-725.
8. H. Jung, S. Y. Lee, C. W. Lee, M. K. Cho, D. H. Won, C. Kim, H.-S. Oh, B. K. Min and Y. J. Hwang, *J. Am. Chem. Soc.*, 2019, **141**, 4624-4633.
9. D. Gao, R. M. Arán-Ais, H. S. Jeon and B. Roldan Cuenya, *Nat. Catal.*, 2019, **2**, 198-210.
10. K. Jiang, R. B. Sandberg, A. J. Akey, X. Liu, D. C. Bell, J. K. Nørskov, K. Chan and H. Wang, *Nat. Catal.*, 2018, **1**, 111-119.
11. Z.-Z. Wu, X.-L. Zhang, Z.-Z. Niu, F.-Y. Gao, P.-P. Yang, L.-P. Chi, L. Shi, W.-S. Wei, R. Liu, Z. Chen, S. Hu, X. Zheng and M.-R. Gao, *J. Am. Chem. Soc.*, 2022, **144**, 259-269.
12. S. Nitopi, E. Bertheussen, S. B. Scott, X. Liu, A. K. Engstfeld, S. Horch, B. Seger, I. E. L. Stephens, K. Chan, C. Hahn, J. K. Nørskov, T. F. Jaramillo and I. Chorkendorff, *Chem. Rev.*, 2019, **119**, 7610-7672.
13. Z. Ni, H. Liang, Z. Yi, R. Guo, C. Liu, Y. Liu, H. Sun and X. Liu, *Coord. Chem. Rev.*, 2021, **441**, 213983.
14. Y. Zheng, A. Vasileff, X. Zhou, Y. Jiao, M. Jaroniec and S.-Z. Qiao, *J. Am. Chem. Soc.*, 2019, **141**, 7646-7659.
15. J. Yu, J. Wang, Y. Ma, J. Zhou, Y. Wang, P. Lu, J. Yin, R. Ye, Z. Zhu and Z. Fan, *Adv. Funct. Mater.*, 2021, **31**, 2102151.
16. T. Luo, K. Liu, J. Fu, S. Chen, H. Li, J. Hu and M. Liu, *J. Energy. Chem.*, 2022, **70**, 219-223.
17. Y. Zhou, Y. Liang, J. Fu, K. Liu, Q. Chen, X. Wang, H. Li, L. Zhu, J. Hu and H. Pan,

Nano Lett., 2022, **22**, 1963-1970.

18. B. Yang, K. Liu, H. Li, C. Liu, J. Fu, H. Li, J. E. Huang, P. Ou, T. Alkayyali and C. Cai, *J. Am. Chem. Soc.*, 2022, **144**, 3039-3049.

19. H. Li, H. Zhou, Y. Zhou, J. Hu, M. Miyauchi, J. Fu and M. Liu, *Chin. J. Catal.*, 2022, **43**, 519-525.

20. A. R. Woldu, Z. Huang, P. Zhao, L. Hu and D. Astruc, *Coord. Chem. Rev.*, 2022, **454**, 214340.

21. B. Sun, M. Dai, S. Cai, H. Cheng, K. Song, Y. Yu and H. Hu, *Fuel*, 2023, **332**, 126114.

22. W. Ma, X. He, W. Wang, S. Xie, Q. Zhang and Y. Wang, *Chem. Soc. Rev.*, 2021, **50**, 12897-12914.

23. F. Hu, L. Yang, Y. Jiang, C. Duan, X. Wang, L. Zeng, X. Lv, D. Duan, Q. Liu, T. Kong, J. Jiang, R. Long and Y. Xiong, *Angew. Chem. Int. Ed.*, 2021, **60**, 26122-26127.

24. Y.-B. Chang, C. Zhang, X.-L. Lu, W. Zhang and T.-B. Lu, *Nano Res.*, 2022, **15**, 195-201.

25. R. B. Sandberg, J. H. Montoya, K. Chan and J. K. Nørskov, *Surf. Sci.*, 2016, **654**, 56-62.

26. Y. Huang, C. W. Ong and B. S. Yeo, *ChemSusChem*, 2018, **11**, 3299-3306.

27. Z. Zhang, L. Bian, H. Tian, Y. Liu, Y. Bando, Y. Yamauchi and Z.-L. Wang, *Small*, 2022, **18**, 2107450.

28. O. Piqué, Q. H. Low, A. D. Handoko, B. S. Yeo and F. Calle-Vallejo, *Angew. Chem. Int. Ed.*, 2021, **60**, 10784-10790.

29. O. Piqué, F. Viñes, F. Illas and F. Calle-Vallejo, *ACS Catal.*, 2020, **10**, 10488-10494.
30. C. Dong, Y. Li, D. Cheng, M. Zhang, J. Liu, Y.-G. Wang, D. Xiao and D. Ma, *ACS Catal.*, 2020, **10**, 11011-11045.
31. M. Peng, C. Dong, R. Gao, D. Xiao, H. Liu and D. Ma, *ACS Central Sci.*, 2021, **7**, 262-273.
32. B. Zhang, Y. Chen, J. Wang, H. Pan and W. Sun, *Adv. Funct. Mater.*, 2022, **32**, 2202227.
33. T. Lu and H. Wang, *Nano Res.*, 2022, **15**, 9764-9778.
34. X. Wei, Y. Liu, X. Zhu, S. Bo, L. Xiao, C. Chen, T. T. T. Nga, Y. He, M. Qiu, C. Xie, D. Wang, Q. Liu, F. Dong, C.-L. Dong, X.-Z. Fu and S. Wang, *Adv. Mater.*, 2023, **35**, 2300020.
35. Y. Liu, Q. Li, R. Si, G.-D. Li, W. Li, D.-P. Liu, D. Wang, L. Sun, Y. Zhang and X. Zou, *Adv. Mater.*, 2017, **29**, 1606200.
36. C. Ling, X. Liu, H. Li, X. Wang, H. Gu, K. Wei, M. Li, Y. Shi, H. Ben, G. Zhan, C. Liang, W. Shen, Y. Li, J. Zhao and L. Zhang, *Angew. Chem. Int. Ed.*, 2022, **61**, e202200670.
37. H. Xu, D. Rebolgar, H. He, L. Chong, Y. Liu, C. Liu, C.-J. Sun, T. Li, J. V. Muntean, R. E. Winans, D.-J. Liu and T. Xu, *Nat. Energy*, 2020, **5**, 623-632.
38. Y. Hori, I. Takahashi, O. Koga and N. Hoshi, *J. Mol. Catal. A: Chem.*, 2003, **199**, 39-47.
39. H. Li, Y. Li, M. T. M. Koper and F. Calle-Vallejo, *J. Am. Chem. Soc.*, 2014, **136**, 15694-15701.

40. I. Ledezma-Yanez, E. P. Gallent, M. T. M. Koper and F. Calle-Vallejo, *Catal. Today*, 2016, **262**, 90-94.
41. W. Zhou, X. Zou, S. Najmaei, Z. Liu, Y. Shi, J. Kong, J. Lou, P. M. Ajayan, B. I. Yakobson and J.-C. Idrobo, *Nano Lett.*, 2013, **13**, 2615-2622.
42. F. Bertoldo, R. R. Unocic, Y.-C. Lin, X. Sang, A. A. Puretzky, Y. Yu, D. Miakota, C. M. Rouleau, J. Schou, K. S. Thygesen, D. B. Geohegan and S. Canulescu, *ACS Nano*, 2021, **15**, 2858-2868.
43. S. Najmaei, J. Yuan, J. Zhang, P. Ajayan and J. Lou, *Acc. Chem. Res.*, 2015, **48**, 31-40.
44. Y. Han, D. Jing, Y. Luan, C.-J. Wang, M. Kolmer, Z. Fei, M. C. Tringides and J. W. Evans, *J. Phys. Chem. Lett.*, 2022, **13**, 6651-6656.
45. D. Jing, A. Lii-Rosales, K. C. Lai, Q. Li, J. Kim, M. C. Tringides, J. W. Evans and P. A. Thiel, *New J. Phys.*, 2020, **22**, 053033.
46. D. Jing, Y. Han, J. W. Evans, M. Kolmer, Z. Fei and M. C. Tringides, *Phys. Rev. Mater.*, 2022, **6**, 094008.
47. G. Shi, L. Yu, X. Ba, X. Zhang, J. Zhou and Y. Yu, *Dalton trans.*, 2017, **46**, 10569-10577.
48. M. Ghosal Chowdhury, L. Sahoo, S. Maity, D. Bain, U. K. Gautam and A. Patra, *ACS Appl. Nano Mater.*, 2022, **5**, 7132-7141.
49. G. Boschetto, S. Carapezzi and A. Todri-Sanial, *ACS App. Electronic Mater.*, 2023, DOI: 10.1021/acsaelm.2c01722.
50. F. Shi, W. Wu, J. Chen and Q. Xu, *Chem. Commun.*, 2021, **57**, 7011-7014.

51. Y. Xie, X. Li, Y. Wang, B. Li, L. Yang, N. Zhao, M. Liu, X. Wang, Y. Yu and J.-M. Liu, *Appl. Surf. Sci.*, 2020, **499**, 143964.
52. Y. Linghu, T. Tong, C. Li and C. Wu, *Appl. Surf. Sci. Appl.*, 2022, **590**, 153001.
53. A. Datar, M. Bar-Sadan and A. Ramasubramaniam, *J. Phys. Chem. C*, 2020, **124**, 20116-20124.
54. K. Kumar, S. Jamnuch, L. Majidi, S. Misal, A. Ahmadiparidari, M. A. Dato, G. E. Sterbinsky, T. Wu, A. Salehi-Khojin and T. A. Pascal, *J. Phys. Chem. Lett.* 2023, **14**, 3222-3229.
55. M. Asadi, B. Kumar, A. Behranginia, B. A. Rosen, A. Baskin, N. Reppin, D. Pisasale, P. Phillips, W. Zhu and R. Haasch, *Nat. commun.*, 2014, **5**, 4470.
56. J. Zhao, D. Liu, F. Wei, W. F. Ip, H. Pan and S. Lin, *Nano Research*, 2023, 1-8. DOI: 10.1007/s12274-023-5718-7.
57. S. A. Francis, J. M. Velazquez, I. M. Ferrer, D. A. Torelli, D. Guevarra, M. T. McDowell, K. Sun, X. Zhou, F. H. Saadi and J. John, *Chem. Mater.*, 2018, **30**, 4902-4908.
58. S. Kang, S. Han and Y. Kang, *ChemSusChem*, 2019, **12**, 2671-2678.
59. G. Kresse and J. Hafner, *Phys. Rev. B*, 1993, **47**, 558-561.
60. G. Kresse and J. Furthmüller, *Phys. Rev. B*, 1996, **54**, 11169-11186.
61. P. E. Blochl, *Phys. Rev. B*, 1994, **50**, 17953-17979.
62. G. Kresse and D. Joubert, *Phys. Rev. B*, 1999, **59**, 1758-1775.
63. J. P. Perdew, K. Burke and M. Ernzerhof, *Phys. Rev. Lett.*, 1996, **77**, 3865-3868.
64. B. Hammer, L. B. Hansen and J. K. Nørskov, *Phys. Rev. B*, 1999, **59**, 7413.

65. S. Grimme, *J. Comput. Chem.*, 2006, **27**, 1787-1799.
66. M. Yu and D. R. Trinkle, *J. Chem. Phys.*, 2011, **134**, 064111.
67. G. J. Martyna, M. L. Klein and M. Tuckerman, *J. Chem. Phys.*, 1992, **97**, 2635-2643.
68. G. Henkelman, B. P. Uberuaga and H. Jónsson, *J. Chem. Phys.*, 2000, **113**, 9901-9904.
69. J. K. Nørskov, J. Rossmeisl, A. Logadottir, L. Lindqvist, J. R. Kitchin, T. Bligaard and H. Jónsson, *J. Phys. Chem. B*, 2004, **108**, 17886-17892.
70. A. A. Peterson, F. Abild-Pedersen, F. Studt, J. Rossmeisl and J. K. Nørskov, *Energy & Environ. Sci.*, 2010, **3**, 1311-1315.
71. P. Calaminici, A. M. Köster, N. Russo and D. R. Salahub, *J. Chem. Phys.*, 1996, **105**, 9546-9556.
72. H. Yang, Y. Wu, Q. Lin, L. Fan, X. Chai, Q. Zhang, J. Liu, C. He and Z. Lin, *Angew. Chem. Int. Ed.*, 2018, **57**, 15476-15480.
73. S. Hanselman, M. T. M. Koper and F. Calle-Vallejo, *ACS Energy Lett.*, 2018, **3**, 1062-1067.
74. K. J. P. Schouten, E. Pérez Gallent and M. T. M. Koper, *ACS Catal.*, 2013, **3**, 1292-1295.
75. V. Sumaria, D. Krishnamurthy and V. Viswanathan, *ACS Catal.*, 2018, **8**, 9034-9042.
76. M. Bajdich, M. García-Mota, A. Vojvodic, J. K. Nørskov and A. T. Bell, *J. Am. Chem. Soc.*, 2013, **135**, 13521-13530.

77. X. Cui, W. An, X. Liu, H. Wang, Y. Men and J. Wang, *Nanoscale*, 2018, **10**, 15262-15272.
78. C. Shi, K. Chan, J. S. Yoo and J. K. Nørskov, *Org. Process. Res. Dev.*, 2016, **20**, 1424-1430.
79. W. Luo, X. Nie, M. J. Janik and A. Asthagiri, *ACS Catal.*, 2016, **6**, 219-229.
80. X. Nie, M. R. Esopi, M. J. Janik and A. Asthagiri, *Angew. Chem.*, 2013, **125**, 2519-2522.
81. X. Nie, W. Luo, M. J. Janik and A. Asthagiri, *J. Catal.*, 2014, **312**, 108-122.
82. C. Shi, K. Chan, J. S. Yoo and J. K. Nørskov, *Org. Process. Res. Dev.*, 2016, **20**, 1424-1430.
83. K. Mathew, R. Sundararaman, K. Letchworth-Weaver, T. Arias and R. G. Hennig, *J. Chem. Phys.*, 2014, **140**.
84. X. Hu, S. Chen, L. Chen, Y. Tian, S. Yao, Z. Lu, X. Zhang and Z. Zhou, *J. Am. Chem. Soc.*, 2022, **144**, 18144-18152.
85. X. Zhang and Z. Zhou, *J. Phys. Chem. C*, 2022, **126**, 3820-3829.
86. T. Liu, Y. Wang and Y. Li, *Adv. Funct. Mater.*, 2022, **32**, 2207110.
87. T. Liu, Y. Jing and Y. Li, *J. Phys. Chem. Lett.*, 2021, **12**, 12230-12234.
88. Y. Sun, Z. Wang, Y. Liu, Q. Cai and J. Zhao, *Inorg. Chem. Front*, 2023, **10**, 2677-2688.
89. Z. Duan and G. Henkelman, *ACS Catal.*, 2019, **9**, 5567-5573.
90. Z. Duan and G. Henkelman, *J. Phys. Chem. C*, 2020, **124**, 12016-12023.
91. Z. Duan and G. Henkelman, *ACS Catal.*, 2020, **10**, 12148-12155.

92. Z. Duan and P. Xiao, *J. Phys. Chem. C*, 2021, **125**, 15243-15250.

93. Z. Duan and G. Henkelman, *ACS Catal.*, 2021, **11**, 14439-14447.